Supporting Information

Gemmell et al. 10.1073/pnas.1306983110

SI Materials and Methods

Swimming Kinematics. Jellyfish (1.5–6 cm) were obtained from the New England Aquarium and maintained in 20-L aquaria at 20 °C. For recording, individual animals were placed into a glass filming vessel (30 × 10 × 25 cm) filled with filtered seawater. Recordings of free-swimming animals were acquired by a high-speed digital video camera (Fastcam 1024 PCI; Photron) at 1,000 frames per second. Only recordings of animals swimming upward were used in the analysis to eliminate the possibly of gravitational force aiding forward motion of the animal between pulses. Therefore, we obtain a more accurate estimate of the contribution of passive energy recapture. Detailed swimming kinematics (2D) were obtained using ImageJ v1.46 software (National Institutes of Health) to track the x and y coordinates of the apex of the jellyfish bell and the tips of the bell margin over time. Swimming speed was calculated from the change in the position of the apex over time as:

$$U = \frac{\left((x_2 - x_1)^2 + (y_2 - y_1)^2\right)^{1/2}}{t_2 - t_1}. \quad \text{[S1]}$$

Jellyfish were illuminated with a laser sheet (680 nm, 2W continuous wave; LaVision) oriented perpendicular to the camera's optical axis to provide a distinctive body outline for image analysis and to ensure the animal remained in-plane, which ensures the accuracy of 2D estimates of position and velocity. To obtain swimming kinematics of large (>6 cm) *Aurelia aurita*, animals were filmed using a high-definition Sony HDV Handycam (model HDR-FX1) at a dedicated off-exhibit tank at the New England Aquarium. Here, a 500-mW laser (432 nm, Hercules series; Laserglow) was formed into a thin sheet to illuminate (from above) the outline of the animal for kinematic analysis.

To demonstrate that inertial motion of *Aurelia* would indeed cease well before the subsequent pulse, and thus show the contribution to swimming distance from passive energy recapture (independent of body inertia), we make a simple estimate based on the equations of ballistic motion. To estimate how far after contraction the jellyfish would travel ballistically, we assign a projectile, with characteristics based on live jellyfish, to have an initial forward velocity equal to the peak velocity measured for the live animal (33.5 mm·s^{-1} for the example in Fig. 3). Assuming the animal is swimming vertically upward, we can ignore the horizontal component and calculate projectile motion from a balance of forces in the vertical direction:

$$\sum F_y = m\frac{dv}{dt} = F_{Drag} - mg. \quad \text{[S2]}$$

Assuming the jellyfish to be a smooth sphere with a diameter equal to that of the animal's bell, Newton's law of motion becomes:

$$\left(m + \frac{1}{2}m_f\right)\frac{dv}{dt} = (m - m_f)g - \frac{\pi}{8}\rho_f v^2 d^2 C_d$$
$$F_{Drag} = \frac{\pi}{8}\rho_f v^2 d^2 C_d, \qquad C_d = \frac{24}{Re^{0.646}}, \qquad Re = \frac{d\rho v}{\eta}, \quad \text{[S3]}$$

where v is the velocity of the jellyfish, d is the bell diameter, m is the mass of the jellyfish, $\frac{1}{2}m_f$ is the added mass of the fluid, ρ_f is the density of seawater, C_D is the instantaneous drag coefficient, and η is the kinematic viscosity of the fluid. We used the fourth-order Runge–Kutta method for computing 2D motion of a body through a fluid, which is detailed by Biringen and Chow (1), to obtain instantaneous position and velocities. A time step Δt of 0.01 s was used, and jellyfish were assigned a ρ of 1,025 m^2·s^{-1} because they are slightly negatively buoyant relative to the water (ρ of 1,020 m^2·s^{-1}). This approximation is based on a static shape, and thus will overestimate where the animal would actually come to rest due to the fact that the live jellyfish is exerting negative propulsive forces during the recovery stroke, which decelerates the animal more quickly (Fig. 3). The fact that we still see the velocity of the jellyfish reach zero well before the next pulse occurs shows that inertia plays a very small role in the motion of the animal between pulses.

Cost of Transport. The metabolic cost of transport (COT) per unit mass and distance (joules per kilogram per meter) for the moon jellyfish (*A. aurita*) was estimated from mass-specific swimming speeds and respiration rates. Mass-specific swimming speeds were obtained from kinematic data (current study) and supplemented with data from Martin (2) and McHenry and Jed (3). Mass-specific active respiration data for *A. aurita* were obtained from a study by Uye and Shimauchi (4). Conversion of metabolic respiration to energy expended (joules) is accomplished by using the conversion factor of 19 J·mL^{-1} of O_2 (5, 6). To obtain net COT, which accounts only for energy expended toward locomotion, basal energy consumption must be subtracted from the active rates. Because basal rates are found to be one-half of the active rates in medusae (6), we calculate the proportion of energy dedicated to location in *Aurelia* as 0.5-fold the active rate. It should be noted that this makes our net $COT_{Aurelia}$ estimates conservative, because pulsation rates in *Aurelia* are lower than in species that were studied by Larson (6). This is because *Aurelia* spends proportionally less time actively contracting compared with many other species (Fig. S1), and because this is the only time energy is expended for swimming, due to passive relaxation (7, 8), the proportion of the active-to-total metabolic rate in *Aurelia* (and COT) will likely be lower. The mass-specific respiration and swimming data for salmon (Fig. 2) were obtained from Brett and Glass (9).

Net COT was calculated using the equation:

$$COT_{Net} = \frac{Energy_{swim}}{Mass \times Velocity}, \quad \text{[S4]}$$

where COT_{Net} is the net COT for runners, fliers, and other swimmers obtained and replotted from studies by Larson (6) and Schmidt-Nielsen (10), using graph digitizing software (GetData v2.25).

Fluid Properties Around Swimming Jellyfish. Fluid motion created by the jellyfish while swimming was quantified using 2D digital particle image velocimetry (DPIV). Using the setup described above, the filtered seawater was seeded with 10-μm hollow glass beads. The velocities of particles illuminated in the laser sheet were determined from sequential images analyzed using a cross-correlation algorithm (LaVision software). Image pairs were analyzed with shifting, overlapping interrogation windows of a decreasing size of 64 × 64 pixels to 32 × 32 pixels or 32 × 32 pixels to 16 × 16 pixels.

Circulation (Γ) of the starting and stopping vortex rings was defined as the vorticity (ω) integrated over the area of the vortex ring, as described by Colin et al. (11), using the equation:

$$\Gamma(t) = \int \omega(x,y,t)dxdy, \qquad \textbf{[S5]}$$

where x and y represent spatial coordinates over a time interval t.

Pressure field data were inferred from the measured velocity fields by numerically integrating the inviscid Navier–Stokes equation, or the Euler equation:

$$\nabla p = -\rho\left(\frac{\partial \mathbf{u}}{\partial t} + (\mathbf{u}\cdot\nabla)\mathbf{u}\right) = -\rho\frac{D\mathbf{u}}{Dt}, \qquad \textbf{[S6]}$$

where ρ is the fluid density and $\mathbf{u}$ is the Eulerian velocity field. Details of this method are given by Colin et al. (11) and are summarized below.

The material acceleration term $\frac{D\mathbf{u}}{Dt}$, which quantifies the acceleration of individual fluid particles in the flow, was calculated from the measured DPIV velocity field $\mathbf{u}(x,y)$. The pressure term was then determined to within a constant of integration by integrating Eq. **S4** spatially. To reduce errors in the numerical integration of the measured velocity data, the procedure of Liu and Katz (12) was used. Data were input using a time series of DPIV data on a 128 × 128 grid. Preprocessing of the DPIV data was completed in MATLAB (MathWorks) to compute the material acceleration $\frac{D\mathbf{u}}{Dt}$, which is also a required input to the pressure calculation code. Material acceleration was determined by computing the difference in the velocity of fluid particles initially located at the DPIV data grid points at time t_1 and subsequently advected to new positions at time t_2 (11). The output data from the code is a time series of pressure fields with scalar pressure computed at each of the 128 × 128 nodes of the corresponding DPIV fields.

To investigate the passive ability of jellyfish mesoglea, during refilling, to enhance stopping vortices and induce flow for energy recapture between pulses, we artificially propelled anesthetized *A. aurita* and measured kinematic motion (ImageJ) and fluid vorticity (DPIV). Animals were anesthetized using a 1:1 mixture of isotonic (14.2 g·L^{-1}) $MgCl_2$ and filtered seawater. This neuromuscular inhibitor blocks transmission of peripheral neuromuscular impulses and had no detrimental effect on the animals and jellyfish, which regained full swimming function within 5 min of being placed in 100% filtered seawater. A manual force was applied to the center of the subumbrellar surface to set the jellyfish in motion. Peak velocities were within 25% of velocities observed in live animals. Acceleration of the bell causes deformation similar to muscular contraction but passively expands and refills the subumbrellar surface, resulting in enhanced vorticity of the stopping vortex and an increase in velocity due to passive energy recapture. Note that exposure to the $MgCl_2$ solution caused the jellyfish to become slightly buoyant; thus, jellyfish were accelerated downward to avoid the additive effect of buoyancy on the kinematic motion.

Kinematic data were log-transformed and checked for normality using a Shapiro–Wilks test. Data were subsequently tested using one-way ANOVA to determine if a significant difference existed between means.

Computational Field Dynamics Model of a Swimming Jellyfish. We developed a jellyfish model using the bell kinematics of an individual 3-cm diameter, free-swimming moon jellyfish (*A. aurita*) as described in the section on swimming kinematics. Kinematics were obtained using a Sony HDV Handycam (model HDR-FX1) and a 500-mW laser. Images were captured at a frequency of 30 frames per second. Because the jellyfish swam straight without any other translation or rotation, we assumed the bell to be axisymmetrical about its central axis and only used one-half of the contour. Digitized points along this half were spatially interpolated using eighth-order polynomials, temporally smoothed using a Butterworth filter, and temporally interpolated using cubic-spline polynomials. The bottom contour of the medusa bell was not always clearly visible in the movie because of obstructive oral arms, so it was approximated by assuming an exponential decrease in bell thickness with increasing top contour arc length. The resulting curve was verified by visual inspection to follow the true bottom contour accurately throughout the contraction and relaxation phases.

The Fluent 13.0 commercial package (ANSYS) was used to solve the unsteady, incompressible, axisymmetrical Navier–Stokes equations. We assumed laminar flow around the jellyfish after calculating a maximum Reynolds number (Re) of 775 based on bell diameter and the marginal fluid velocity of 2 cm·s^{-1} predicted for a 3-cm *A. aurita* (13). The Pressure Implicit solution by Split Operator method pressure-velocity coupling algorithm was used with second-order spatial and first-order transient discretizations, and residuals were reduced by three orders of magnitude at each time step. The equations were solved on a numerical domain measuring six bell diameters in the radial direction and 16 bell diameters in the axial direction, with the jellyfish initially positioned 10 bell diameters from the inlet (Fig. S3). Swimming kinematics were prescribed to the jellyfish by user-defined functions that moved the bell surface nodes at each time step. Because these kinematics cause large bell deformations, both dynamic mesh smoothing and remeshing were used to maintain acceptable mesh quality throughout the simulation.

Swimming was modeled by coupling the forward motion of the jellyfish to the hydrodynamic forces exerted on the bell. Pressure and shear forces acting in the axial direction were integrated across the jellyfish surface at the end of each time step, and the resulting body acceleration was calculated. The discrete form of this force balance is given by the equation:

$$\sum F_z^n = m\left(\frac{d^2z}{dt^2}\right)^n, \qquad \textbf{[S7]}$$

where $\sum F_z^n$ is the sum of all pressure and shear forces in the axial direction at time step n, m is the mass of the jellyfish (fluid density assumed to be the same as the surrounding water: ρ = 998.2 kg·m^{-3}), and $\left(\frac{d^2z}{dt^2}\right)^n$ is the axial acceleration at the center of mass of the jellyfish. Using Taylor series expansions, the acceleration can be approximated by a second-order accurate, backward finite difference equation:

$$\left(\frac{d^2z}{dt^2}\right)^n \approx \frac{2z^n - 5z^{n-1} + 4z^{n-2} - z^{n-3}}{(\Delta t)^2}, \qquad \textbf{[S8]}$$

where z is the axial displacement and Δt is the time step. Combining Eqs. **S7** and **S8**, the displacement at time step n can be approximated:

$$z^n \approx \frac{(\Delta t)^2 \sum F_z^n}{2m} + \frac{5}{2}z^{n-1} - 2z^{n-2} + \frac{1}{2}z^{n-3}. \qquad \textbf{[S9]}$$

Finally, to ensure stable coupling between the solver and the jellyfish displacement, we used an exponentially weighted moving average to smoothen the raw displacement z^n:

$$\zeta^n = \begin{cases} z^n, & n = 0 \\ \alpha\ z^n + (1-\alpha)\ \zeta^{n-1}, & n > 0 \end{cases}, \qquad \textbf{[S10]}$$

where ζ is the smoothed displacement prescribed to the jellyfish and $\alpha \in [0, 1]$ is the smoothing factor. We found $\alpha = 0.25$ was required for a robust simulation.

Verification and validation studies were performed to ensure the numerical and physical accuracy of our simulation. We first checked the sensitivity of our results to mesh and time step refinement (Fig. S4). A base mesh of 60,895 cells (64 and 58 cell faces on the top and bottom bell contours, respectively) was refined to 135,765 cells (86 and 82 cell faces on the top and bottom bell contours, respectively) and showed that the sum of forces acting on the jellyfish, and consequently its swimming performance, was insensitive to spatial refinement. Similarly, simulations run using a time step refined from $\Delta t = 1/90$ s to $\Delta t = 1/180$ s resulted in no appreciable change in the hydrodynamic forces acting on the jellyfish. Next, the instantaneous displacement of the numerical jellyfish was compared with the natural jellyfish used for the swimming kinematics (Fig. S5). Both show similar trends and indicate similar velocities throughout the swimming period, resulting in a nearly identical total displacement.

SI Discussion

It is important to note that although all the slopes of the regression lines in Fig. 1*A* are negative, indicating a reduction in COT with body size, the slope of the regression line for *Aurelia* is shallower than for other propulsors. One reason for this stems from the fact that average swimming speeds for large jellyfish are not size-dependent (14, 15). As *Aurelia* grows beyond ≈20 cm in diameter, swimming speed remains relatively constant (14). Like other scyphomedusae (16), larger *Aurelia* have a slower bell contraction rate than do smaller ones but move farther per contraction. The two processes roughly balance, producing similar speeds for most large individuals. This can act to shallow the slope of the regression line and, in the case of another jellyfish (*Stomolophus meleagris*), to produce a distinguishable curvilinear relationship (Fig. 1*D*) (15). The inability of jellyfish to continue increasing swimming velocity with size is a function of their unique muscle arrangement. The single cell layer of muscle limits the thickness of swimming muscles within cnidarians, and thus force production during medusan swimming. As a result, the additional force required to continue increasing swimming speed with body size is limited to a specific range in jellyfish. This has consequences with respect to COT because jellyfish appear to have the greatest advantage over other metazoans when they are small. However, extrapolating the results from Fig. 1 indicates that fish only begin to exhibit a lower COT than *Aurelia* beyond a body mass of approximately 100 Kg.

Large differences in distance gained during stopping vortex energy recapture were observed among species (Fig. 3 and Fig. S2). We find that during normal (cruising) swimming, the more oblate scyphomedusae (*Aurelia*) exhibits the largest boost with 32.3% (SD = 6.0), 29.7% (SD = 8.6), and 29.1% (SD = 6.8) for 2-cm, 5-cm, and 10-cm animals, respectively, of the total distance per pulse coming from the interpulse duration. No difference was observed between sizes ($P = 0.55$). The conservation of the effect of passive energy recapture suggests that a significant amount of distance can be gained per pulse even at larger body sizes, which may be important to consider for bioinspired design. Rhizostomes exhibited significantly lower distances ($P < 0.001$), with *Catostylus* and *Phyllorhiza* observed to gain 8.9% (SD = 5.8%) and 10.8% (SD = 1.6%) per pulse, respectively. The hydromedusa *Eutonina* has a pulse frequency between that of the rhizostomes and *Aurelia* (Fig. 2) and also displays an intermediate proportion of the total distance gained during the interpulse duration at 19.6% (SD = 7.0%).

Rhizostomes showed a significantly ($P < 0.001$) shorter duration between pulses compared with *Aurelia* (Fig. 3). Because this part of the swimming cycle is when passive energy recapture can occur, it raises the question of why some species do not appear to take full advantage of such a mechanism. The answer may be related to feeding mechanisms. Rhizostome jellyfish must move water at relatively high velocities through a dense array of feeding structures on the oral arms to capture small prey items (17). These densely arranged feeding structures require relatively high Re flow to move water through food-capturing surfaces. Thus, a high pulse rate that minimizes the time between pulses can ensure that high-velocity water moves more frequently through capture surfaces, and feeding rates can be maximized. In this case, the significant decrease in distance gained from the energy recapture of the stopping vortex may represent a tradeoff between swimming efficiency and food capture. Jellyfish species that require a consistently high Re to bring prey in contact with capture surfaces may represent a tradeoff between feeding and swimming efficiency. This may explain why some species (e.g., *Aurelia*) that do not require consistently high flow to contact prey exhibit a greater contribution of energy recapture during swimming. Alternatively, the fact that some rhizostome jellyfish frequently migrate or exhibit directed swimming (16) may require sacrificing efficiency for greater mean swimming velocities.

Pulsation rates in jellyfish are known to vary with animal size (16) but can also vary instantaneously among individuals with a shadow/startle response (18) or when physically contacted (14). Here, a higher pulse rate approximately equal to threefold that of normal swimming (Fig. S2) may indicate some form of avoidance/escape swimming whereby velocity is gained at the expense of efficiency. Indeed, a significant ($P < 0.001$) drop in distance during interpulse durations is clearly observed in *Aurelia* (Fig. 3*A*). However, the rapid contractions of a startled *Aurelia* resulted in a mean swimming velocity of 10.3 $mm{\cdot}s^{-1}$ (SD = 0.3) compared with 8.9 $mm{\cdot}s^{-1}$ (SD = 1.3) during normal swimming. Although the significance of a modest increase of 15% in velocity observed by increasing pulse rates by ≈300% is uncertain, it does demonstrate the ability to modulate the influence of passive energy recapture on an individual basis in jellyfish.

Experiments with anesthetized 4-cm *A. aurita* in which animals were artificially propelled forward at natural swimming velocity and then allowed to drift freely confirmed that passive expansion/refilling occurs in this species and allowed observation of stopping vortex influence beyond the duration at which the subsequent contraction normally begins (Fig. S1). Here, we confirm that anesthetized animals decelerate and expand similar to non-anesthetized animals (Fig. S1 and Movie S2) due to elastic recoil. We find the thrust created by stopping vortices has the potential to carry a 4-cm *Aurelia* an additional 10.1 mm (SD = 0.8, $n = 4$) each pulse. However, *Aurelia*, when not anesthetized, only travels an additional 4.4 mm (SD = 0.7, $n = 5$) or 43% of each pulse. Interestingly, timing of the subsequent contraction coincides near the maximum velocity applied to the jellyfish by the stopping vortex (Fig. S1). By contracting around the time of maximum velocity, *Aurelia* starts the next contraction with maximal momentum offered by the stopping vortex. This prevents the animal from starting locomotion from rest with each pulse and can lead to greater swimming velocity in the subsequent pulse (Fig. 3*B*). Also, the remaining circulation may play a more significant role during interaction with the subsequent starting vortex, and using 100% of this energy between pulses would result in very low average velocities due to the length of time (>4 s for a 4-cm *A. aurita*) it would take the stopping vortex to dissipate fully at a moderate to high Re (Fig. 3*D*).

The result of refilling of the bell during expansion enhances vorticity and circulation of the stopping vortex (Fig. 2*A* and Movie S1). Vortex rings create an induced jet (19), and the jet flow is directed at the subumbrellar surface of the jellyfish in this case. After refilling, we observe elevated pressure in this region relative to the exumbrellar surface using both computational fluid dynamics (CFD) and a unique empirically based technique based on velocity fields (Fig. 4). CFD simulation shows lower velocity and a weaker boost in velocity from passive recapture of energy from the vortex ring compared with our experimental measurements. Although the effect of passive energy capture

is still clearly observed using CFD, the effect is dampened slightly from digitization of a randomly selected swimming sequence that was likely not at steady state. In addition, the animal used for the CFD simulations was smaller than in the empirical comparison. However, both CFD and the empirically based method of pressure estimation provide a mechanistic explanation of how passive refilling of the bell can create positive thrust during a period when no kinematic motion is occurring. This translates into forward velocity using little or no addition energy and acts to reduce COT, making jellyfish one of the most efficient propulsors on earth. The only organism known to display a COT similar to that of *Aurelia* is an eel that migrates 5,000–6,000 km into the Sargasso Sea (20). These fish swim four- to sixfold times more efficiently than non–eel-like fish.

Medusae have persisted for over 452 million years (21), and as one of the first metazoans to swim using muscles (22), they have developed several mechanisms to aid in propulsion. In addition, vortices produced by rowing-type medusae are known to remain in the tentacle region roughly 10-fold as long as those produced by jetting medusae (23). This leads to an increased ability to extract food from the water, and thus more energy available to for growth and reproduction. With so little spent on locomotion, and thus encountering prey, passive energy recapture is likely a contributing factor to the ability of some jellyfish populations to bloom rapidly over short periods. In addition, the fact that passive energy recapture appears to scale well with animal size suggests there are important implications to be explored for bioinspired design over a wide range of size scales up to 100 kg.

1. Biringen S, Chow C-Y (2011) *Flow Topics Governed by Ordinary Differential Equations: Initial-Value Problems. An Introduction to Computational Fluid Mechanics by Example* (John Wiley & Sons, Inc., Hoboken, NJ), pp 1–49.
2. Martin LE (2001) Limitations on the use of impermeable mesocosms for ecological experiments involving *Aurelia* sp. (Scyphozoa: Semaeostomeae). *J Plankton Res* 23(1):1–10.
3. McHenry MJ, Jed J (2003) The ontogenetic scaling of hydrodynamics and swimming performance in jellyfish (*Aurelia aurita*). *J Exp Biol* 206(Pt 22):4125–4137.
4. Uye S, Shimauchi H (2005) Population biomass, feeding, respiration and growth rates, and carbon budget of the scyphomedusa *Aurelia aurita* in the inland Sea of Japan. *J Plankton Res* 27(3):237–248.
5. Elliott JM, Davison W (1975) Energy equivalents of oxygen consumption in animal energetics. *Oecologia* 19(3):195–201.
6. Larson RJ (1987) Trophic ecology of planktonic gelatinous predators in Saanich Inlet, British Columbia: Diets and prey selection. *J Plankton Res* 9(5):811–820.
7. Megill WM, Gosline JM, Blake RW (2005) The modulus of elasticity of fibrillin-containing elastic fibres in the mesoglea of the hydromedusa *Polyorchis penicillatus*. *J Exp Biol* 208(Pt 20):3819–3834.
8. Demont ME, Gosline JM (1988) Mechanics of jet propulsion in the hydromedusan jellyfish, *Polyorchis pexicillatus*: I. Mechanical properties of the locomotor structure. *J Exp Biol* 134(1):313–332.
9. Brett JR, Glass NR (1973) Metabolic rates and critical swimming speeds of sockeye salmon (*Oncorhynchus nerka*) in relation to size and temperature. *J Fish Res Board Can* 30(3):379–387.
10. Schmidt-Nielsen K (1972) Locomotion: Energy cost of swimming, flying, and running. *Science* 177(4045):222–228.
11. Colin SP, et al. (2012) Biomimetic and live medusae reveal the mechanistic advantages of a flexible bell margin. *PLoS ONE* 7(11):e48909.
12. Liu X, Katz J (2006) Instantaneous pressure and material acceleration measurements using a four-exposure PIV system. *Exp Fluids* 41(2):227–240.
13. Costello JH, Colin SP (1994) Morphology, fluid motion and predation by the scyphomedusa *Aurelia aurita*. *Marine Biology* 121(2):327–334.
14. Hamner WM, Hamner PP, Strand SW (1994) Sun-compass migration by *Aurelia aurita* (Scyphozoa): Population retention and reproduction in Saanich Inlet, British Columbia. *Marine Biology* 119(3):347–356.
15. Larson RJ (1987) Costs of transport for the scyphomedusa *Stomolophus meleagris* L. Agassiz. *Can J Zool* 65(11):2690–2695.
16. Hamner W, Hauri I (1981) Long-distance horizontal migrations of zooplankton (Scyphomedusae: *Mastigias*). *Limnol Oceanogr* 26(3):414–423.
17. D'Ambra I, Costello J, Bentivegna F (2001) Flow and prey capture by the scyphomedusa *Phyllorhiza punctata* von Lendenfeld, 1884. *Hydrobiologia* 451(1-3):223–227.
18. Arkett SA (1985) The shadow response of a hydromedusan (*Polyorchis penicillatus*): Behavioral mechanisms controlling diel and ontogenetic migration. *Biol Bull (Woods Hole, MA)* 169(2):297–312.
19. Drucker EG, Lauder GV (1999) Locomotor forces on a swimming fish: Three-dimensional vortex wake dynamics quantified using digital particle image velocimetry. *J Exp Biol* 202(Pt 18):2393–2412.
20. van Ginneken V, et al. (2005) Eel migration to the Sargasso: Remarkably high swimming efficiency and low energy costs. *J Exp Biol* 208(Pt 7):1329–1335.
21. Wade M (1969) Medusae from uppermost Precambrian or Cambrian sandstones, Central Australia. *Palaeontology* 12(3):351–365.
22. Valentine JW (2004) *On the Origin of Phyla* (Univ of Chicago Press, Chicago).
23. Lipinski D, Mohseni K (2009) Flow structures and fluid transport for the hydromedusae *Sarsia tubulosa* and *Aequorea victoria*. *J Exp Biol* 212(Pt 15):2436–2447.

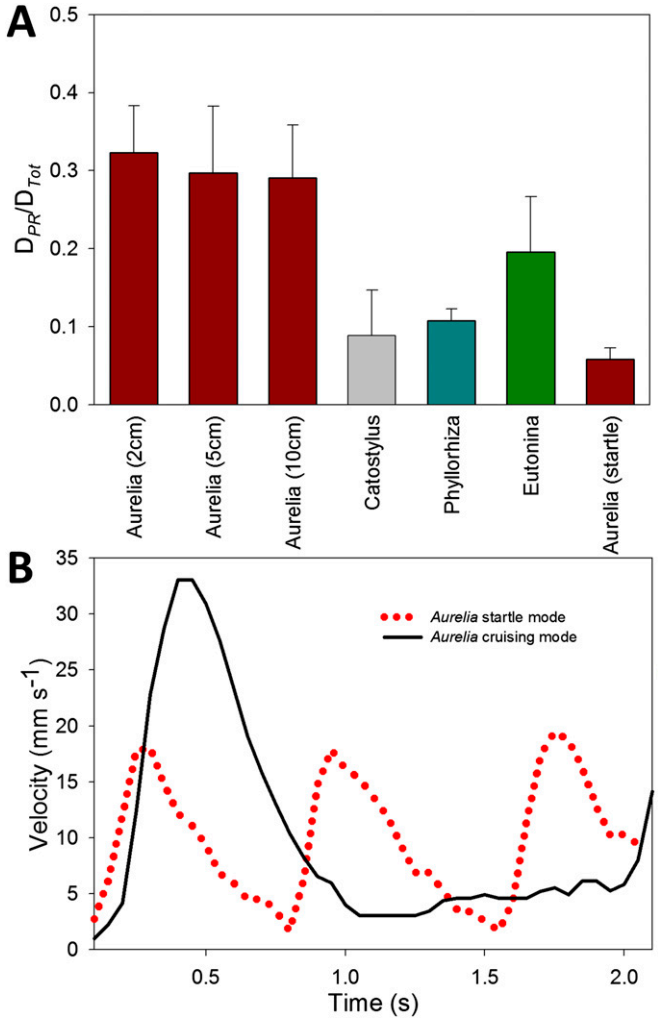

Fig. S1. Variation in the amount of distance gained from passive energy recapture for different sizes, behavioral response of *A. aurita*, and among other species. (*A*) Proportion of the distance traveled during the postrecovery phase of the swimming cycle relative to the total distance of the swimming cycle. D_{PR}, distance traveled from passive energy recapture; D_{Tot}, total distance traveled per swimming stroke. (*B*) Difference in swimming performance and timing of contractions for *A. aurita* during normal (cruising) locomotion vs. a startle response.

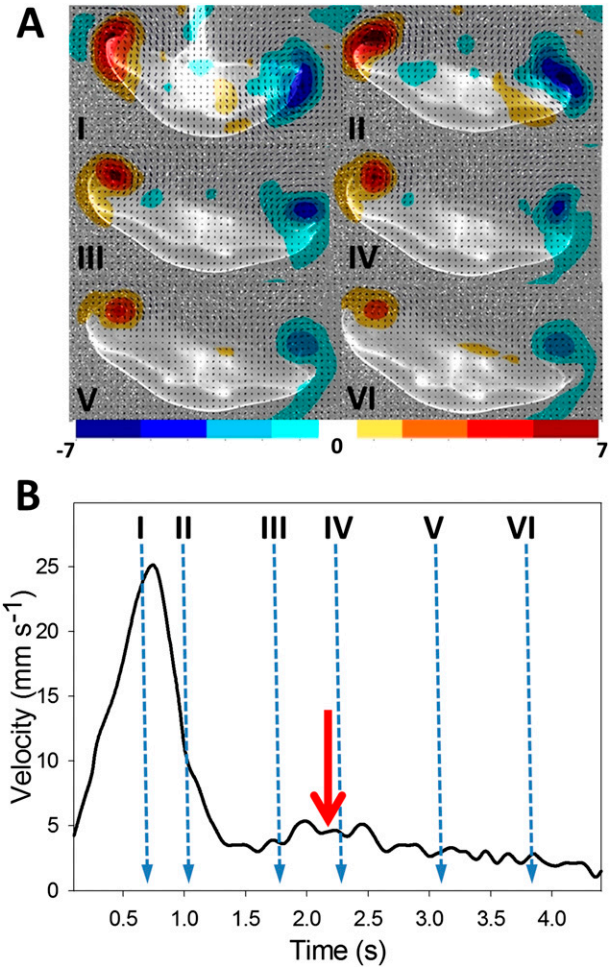

Fig. S2. Anesthetized *A. aurita* artificially propelled forward to investigate passive thrust generation. (*A*) Time series plot (I–VI) shows change in vorticity over time. (Note: Animals had slight positive buoyancy in the anesthetic solution, and thus were not simply moving due to gravity.) (Scale bar, 3 cm.) (*B*) Performance plot with time steps from *A* noted. The red arrow corresponds to the average time at which the subsequent contraction begins in nonanesthetized animals.

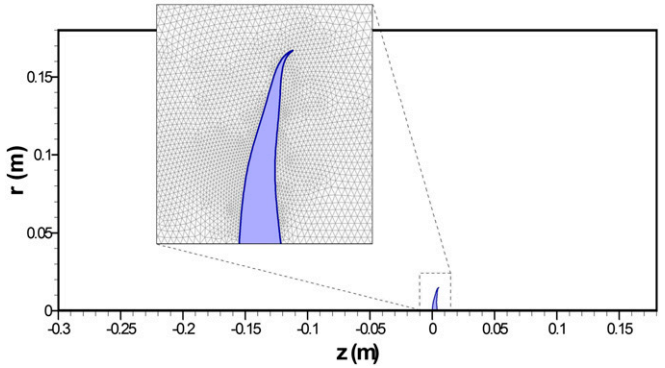

Fig. S3. CFD simulations were solved on a numerical domain measuring 18 cm (6 bell diameters) in the radial direction and 48 cm (16 bell diameters) in the axial direction with an unstructured, body-fit mesh refined in the vicinity of the jellyfish. A zero velocity boundary condition was assigned at the inlet (left boundary), and a zero pressure boundary condition was assigned at the outlet (right boundary). The outer radial boundary was treated as a free-slip wall, and the inner boundary was assigned as the axis of symmetry along which the jellyfish was free to slide. The jellyfish was treated as a no-slip wall.

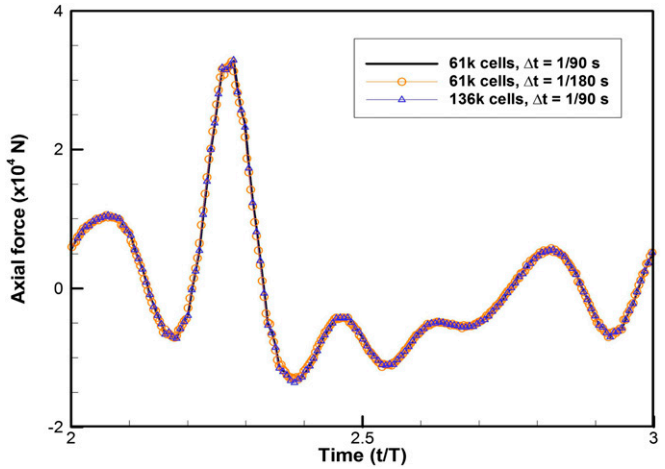

Fig. S4. Simulation was verified by checking the sensitivity of results to mesh and time step refinement. Shown is the fluctuation of our parameter of interest, the axial forces acting on the jellyfish, during one swimming period ($T = 1.7$ s). Cases run on the base mesh and time step (61,000 cells, $\Delta t = 1/90$ s) produced nearly identical results to those run on a refined initial mesh (136,000 cells) with refined remeshing parameters and those run with a refined time step (1/180 s). Therefore, convergence of the parameter was achieved with the base conditions.

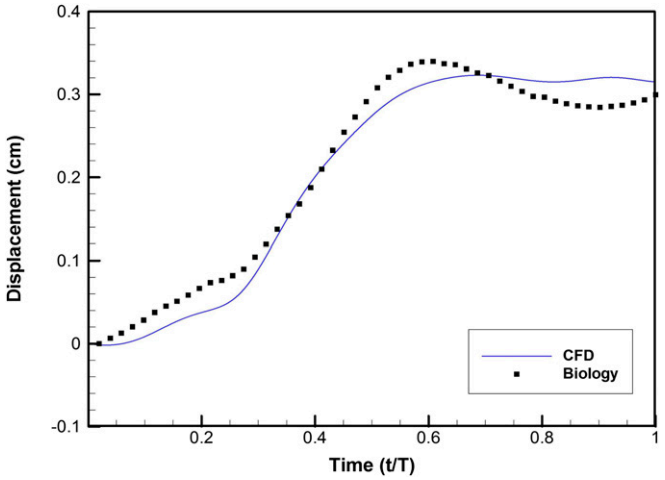

Fig. S5. Axial swimming displacement of the natural jellyfish used for modeling compares well with the result of its simulation. Similar characteristics are seen in both, such as a rapid increase in displacement during the contraction phase starting at $t/T = 0.3$, backward motion during the relaxation phase around $t/T = 0.7$, and a final increase in displacement at the end of the swimming period. Further, total displacements at the end of the swimming period are nearly identical, as well as maximum velocities achieved during contraction. Discrepancies are likely caused by natural asymmetry not taken into account by the kinematics or the fluid results.

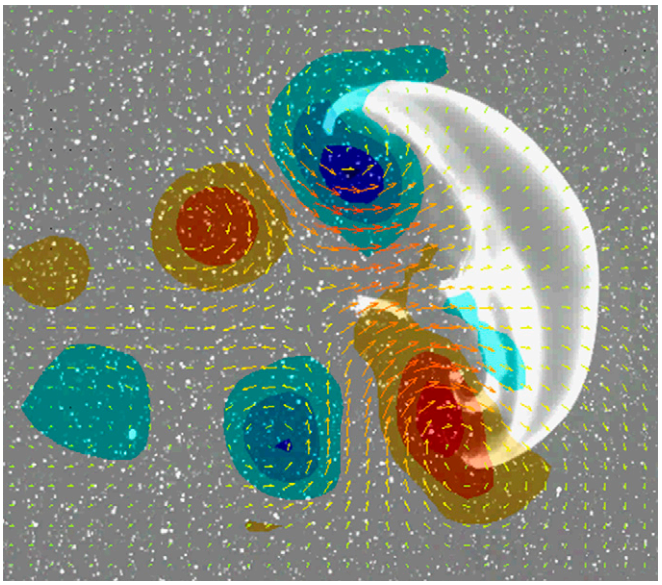

Movie S1. DPIV of a 2-cm *A. aurita* jellyfish shows the velocity vectors and vorticity produced by swimming. Notice how the stopping vortex forms upstream and on the exumbrellar surface of the animal before recovery. The vortex ring then moves under the bell as its vorticity (energy) increases.

Movie S1

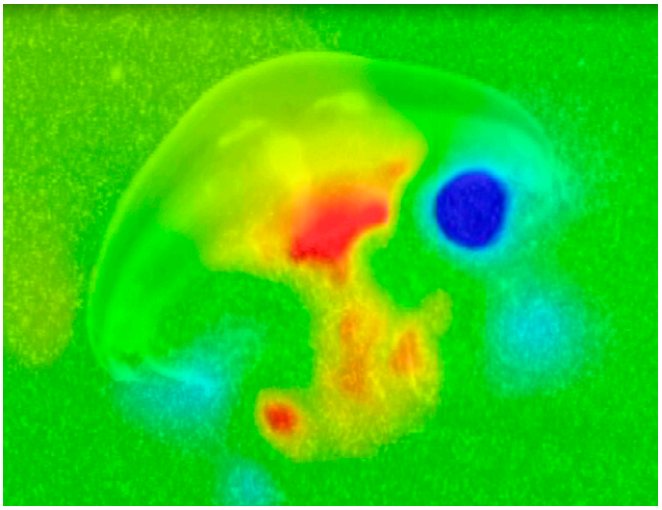

Movie S2. Instantaneous pressure field estimations are shown simultaneously with body velocity to demonstrate a mechanistic explanation for how jellyfish can accelerate, and thus gain extra distance, during a period of the swimming cycle in which there is no kinematic motion.

Movie S2